Incoherent control of two-photon induced optical measurements in open quantum systems: Quantum heat engine perspective

Md Qutubuddin and Konstantin E. Dorfman*

State Key Laboratory of Precision Spectroscopy, East China Normal University, Shanghai 200062, China
and Himalayan Institute for Advanced Study, Unit of Gopinath Seva Foundation, MIG 38, Avas Vikas, Rishikesh, Uttarakhand 249201, India

(Received 9 December 2021; accepted 10 May 2022; published 30 June 2022)

We present a consistent optimization procedure for the optical measurements in open quantum systems using recently developed incoherent control protocol. Assigning an effective hot bath for the two-entangled-photon pump we recast the transmission of classical probe as a work in a quantum heat engine framework. We demonstrate that maximum work in such a heat engine can exceed that for the classical two-photon and one-photon pumps, while efficiency at maximum power can be attributed to conventional boundaries obtained for the three-level maser heat engine. Our results pave the way for incoherent control and optimization of optical measurements in open quantum systems that involve two-photon processes with quantum light.

DOI: 10.1103/PhysRevResearch.4.023259

I. INTRODUCTION

A Thermal engine [1] plays a pivotal role in many thermodynamical processes. In the seminal work by Scovil and Schulz-DuBois [2], a maser heat engine was formulated in the context of the detailed balance which results in the maximum efficiency [3,4] for a three level system [5–8] operating between hot and cold baths. The ascent of quantum heat engines (QHEs) has attracted a significant amount of attention in the last few decades and constitutes an important research direction within quantum thermodynamics, both theoretically [9–18] and experimentally [19–24]. In addition to the diverse development of QHEs [25–27], they have intrinsic relationships with real physical systems such as lasers, solar cells [28,29], batteries [15,30], light harvesting [31], etc. While some of the promising features of QHEs such as quantum coherence and entanglement [32–35] show a possibility for enhancing the maximum output power for resonantly driven systems [36], the significance of entanglement in optical measurements in open quantum systems from the QHE perspective has not been investigated so far.

Recently, the authors developed an incoherent control method of optical signals [37] that views the pump-probe measurements as a QHE, which transfers energy from the pump pulse to the probe pulse, treating the dissipation to the environment explicitly, while computing the work performed by the system via the detected probe photons. In this method we have introduced an effective thermal bath by combining a coherent pump pulse excitation of electronic excited states of molecules with the thermal relaxation. The "incoherent" control algorithm for the optical signals in open quantum systems is then introduced based on the analogy with the QHE. It has been further shown that the spectroscopic measurement for the probe pulse transmission can be improved when the corresponding parameter regime is close to a limit of operation, such as the Curzon-Ahlborn limit, etc. Note, that incoherent control has been introduced in the context of numerical optimization of coherent optical measurements [38]. Our method is fully analytical and is based on the analogy with the quantum thermodynamics.

In the course of the above developments we realized that the efficient operation of QHEs in open quantum systems such as molecules is strongly correlated with the ability to efficiently excite a particular electronic state. At the same time the various molecular degrees of freedom such as nuclear motion, the complex selection rules, and the associated dissipation processes restrict the ability to control the excited states' probabilities. Moreover the latter are governed by the uncertainty relation between the spectral bandwidth of the molecules and the temporal profile of the excitation pulse. It has been further shown that two-photon excitation with the entangled photons can efficiently control the multiexciton population distribution in complex molecules since these can violate the uncertainty principle in the two-photon absorption measurements [39]. In addition to the spectral selectivity, the entangled two-photon absorption probability scales linearly with the pump intensity, in contrast with the classical two-photon absorption which is quadratic in the pump intensity [40]. This feature makes it attractive for the low intensity applications in the photosensitive materials such as biological molecules, etc. [41]. While a significant amount of experimental [42] effort has been dedicated to the optimization of two-photon absorption measurement using quantum light, it lacks a formalized theoretical foundation due to the dissipative nature of the open quantum system. It is therefore imperative to develop a consistent optimization procedure for such optical measurements in connection with the fundamental frameworks such as QHEs.

*dorfmank@lps.ecnu.edu.cn

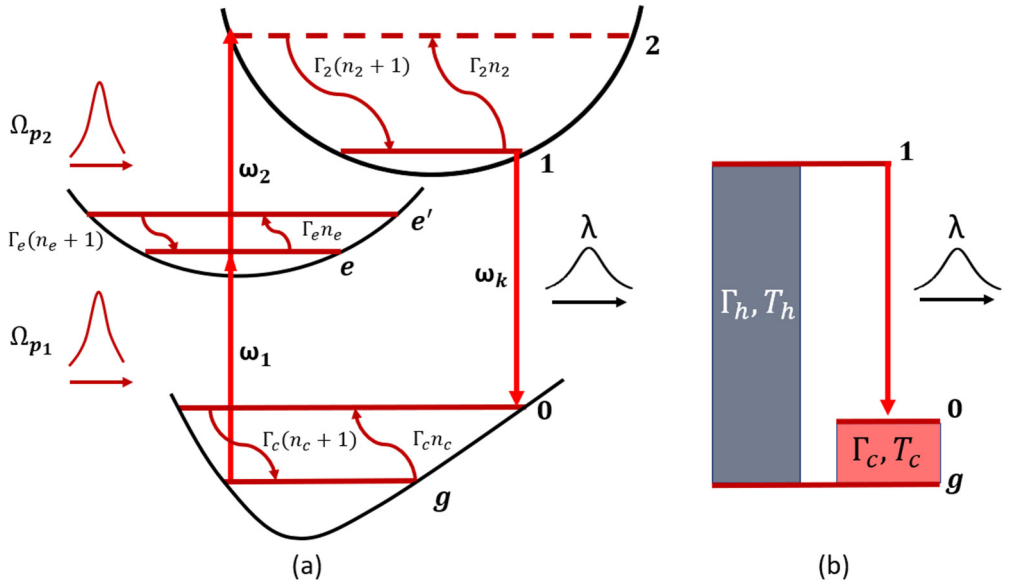

FIG. 1. (a) Schematic for the three-level molecule undergoing two-photon pump-probe measurements. The pump field resonant with transition g–2 excites a vibrational wave packet in the higher vibrational state 2 via the intermediate levels e and e', which relaxes to the lower energy vibrational state 1. The probe field then stimulates the emission from the state 1 to the excited vibrational level 0 in the ground electronic state. Finally, vibrational relaxation brings the system back to its ground state g. (b) Equivalent three-level QHE with transitions between energy levels g–1 and g–0 driven by hot (at temperature T_h) and cold (at T_c) heat baths. The single-mode stimulated emission representing the work done by the QHE occurs at the 1–0 transition with the Rabi frequency λ.

In this article we explore the QHE analogy with a setup that involves two-photon pump excitation with both classical and quantum states of light by utilizing an effective thermal bath [37]. The two photons can be initially in, e.g., an entangled twin photon state, which allows us to explore the effects of entanglement in QHE operation. By presenting a consistent technique of maximization of power and efficiency at maximum power for the two-photon pumped QHE using incoherent control, one can manipulate the two-photon induced fluorescence (TPIF) and pump-probe signals due to an additional control parameter (entanglement time) [39,43] which does not exist classically.

II. EFFECTIVE HEAT BATH

We consider a three-level molecular system with ground state g, single excited electronic state e, and double excited electronic state f (see Fig. 1). To keep the notations consistent with our previous work [37] we denote vibrational states of the electronic ground state as 0 and g, while vibrational states of the double excited electronic state are 2 and 1, and e and e' denote vibrational states of the single excited electronic state. A two-photon pump field excites a molecule from g to 2 via states e and e' with the pump Rabi frequencies Ω_i and central frequencies ω_i, $i = 1, 2$. The vibrational state 2 relaxes to 1 by emission of a phonon. The stimulated emission 1–0 due to interaction with a probe field of Rabi frequency λ is followed by thermal relaxation via interaction of the 0–g transition with the cold bath, which then brings the system to its initial ground state. The total Hamiltonian of the system is given by

$$\hat{H}_{\text{tot.}} = \hat{H}_0 + \hat{H}_I + \hat{H}_{I.V.}, \tag{1}$$

where subscript I indicates the light-matter interaction of pump and probe fields and $I.V.$ indicates the interaction with the vibrational modes; $\hat{H}_0 = \sum_i \omega_i |i\rangle\langle i|$, where $i = g, 0, e, e', 1, 2$. The pump-molecule interaction Hamiltonian in the rotating wave approximation reads

$$\hat{H}_I(t) = -\hat{V}^\dagger(t) \sum_{i=1,2} (\hat{E}_j(t) + \hat{E}_j^\dagger(t)), \tag{2}$$

where $\hat{V}(t) = \mu_{ge}\ e^{-i\omega_e t}\ |g\rangle\langle e| + \mu_{e2}\ e^{-i\omega_2 t}\ |e\rangle\langle 2|$, and $\hat{E}_j(t) = i\int_0^\infty d\omega_j \sqrt{\frac{\hbar\omega_j}{2\mathbf{V}\epsilon_0}}\hat{a}_j(\omega_j)e^{-i\omega_j t}$, where $j = 1, 2$, indices denote the first and second photons, $\hat{a}_j$ and $\hat{a}_j^\dagger$ are the annihilation and creation operators for the jth photon that satisfy the commutation relation $[\hat{a}_j(\omega), \hat{a}_{j'}^\dagger(\omega')] = \delta(\omega - \omega')\delta_{jj'}$, $\mathbf{V}$ is the quantization volume, and $H_{I.V} = \sum_{m,i<j} b_m^\dagger |i\rangle\langle j| e^{-i\omega_i t}$. The two-photon pump utilized in our work originates from the single photon sources so the coupling to the system is naturally weak. In the case of multiphoton sources such as squeezed light the coupling can be moderate, yet it is far from being strong [44]. Hence, we consider that the couplings to the pump fields are weak so we can use the perturbation theory.

Assuming that all molecules are initially in the ground state, the density matrix of the interacting matter-field system at time t is given in the interaction picture by the time-ordered exponential superoperator

$$\hat{\rho}(t) = \hat{\mathcal{T}} \exp\left[-\frac{i}{\hbar}\int^t dt' \hat{H}_{\text{int},-}(t')\right]\hat{\rho}_{\text{mat}} \otimes \hat{\rho}_{\text{field}}, \tag{3}$$

where $\hat{\mathcal{T}}$ is a time ordering superoperator, the interaction Hamiltonian superoperator $\hat{H}_{\text{int},\pm}$ is defined by its action on the ordinary operator $\hat{X}$ as $\hat{H}_{\text{int},-}\hat{X} = \hat{H}_{\text{int}}\hat{X} - \hat{X}\hat{H}_{\text{int}}$ and $\hat{H}_{\text{int},+}\hat{X} = \hat{H}_{\text{int}}\hat{X} + \hat{X}\hat{H}_{\text{int}}$ [45], $\hat{\rho}_{\text{field}}$ denotes the ground state

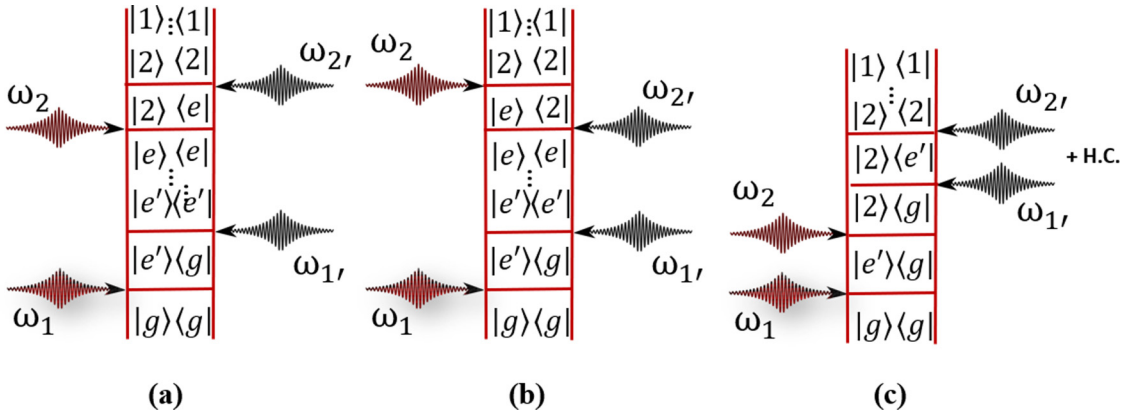

FIG. 2. (a) The set of double sided Feynman diagrams representing the leading order contribution to the population of excited state due to relaxation 2–1. There are a total of six pathways that contribute to the matter field system: diagrams (a)–(c) and their complex conjugates.

of the matter system, and $\hat{\rho}_{\rm mat}$ denotes the initial state of the light field. The leading-order contribution to the population of level 1 is given by the convolution of four-point field and matter correlation functions using the Feynman diagram in Fig. 2, obtained from Eqs. (A17), (A18), and (A19) in Appendix A. The total population of state 1 due to pumping transition g–2 followed by the relaxation $2-1$ is given by $\rho_{11}(t) = \rho^a_{11}(t) + \rho^b_{11}(t) + \rho^c_{11}(t)$, obtained from Eq. (A20), and it is recast by introducing the detuning $\delta = \omega_{2e} - \omega_{2e'}$ and assuming the pump is tuned midway between e and e' states, $\omega_0 = \frac{1}{2}(\omega_{2e'} + \omega_{2e})$. The solution we obtain for the population of level 1 from Eq. (A20) reads

$$\rho_{11}(t) = \frac{16\,\delta^2\,\tilde{\delta}^2\,\Omega_p^4(1 - e^{-\Gamma_2(2n_2+1)})}{(2n_2+1)\big(\delta^2 + 4\sigma_p^2\big)^2\big(\tilde{\delta}^2 + 4\sigma_p^2 + \big)^2},$$
$$\rho_{gg}(t) = 1 - \rho_{11}(t), \tag{4}$$

where $\tilde{\delta} = \delta + 2\omega_{2e'} - 2\omega_{e'g}$. Before proceeding to the QHE model, which is based on the perturbative solution of the complete set of equations given by Eq. (A21) (Appendix A), we first introduce an effective heat bath. To that end, we assume that the probe field is much stronger than the coupling to the phonon bath that governs the 2–1 transition, which itself is stronger than that of the bath driving the 0–g transition: $\lambda \gg \Gamma_2 n_2 \gg \Gamma_c n_c$. The latter condition can be obtained in a variety of molecular systems [46]. Under these conditions one can eliminate the state 0 from the total system of Eq. (A21) and consider only the three states such that the combined effect of the coherent excitation g–2 is followed by a relaxation 2–1 in Fig. 1(b) can be replaced by an effective thermal bath at temperature T_h with the average photon number $n_h = [\exp(\omega_{1g}/T_h) - 1]^{-1}$ and dephasing Γ_h. In this case the state 2 can be eliminated and the corresponding equation of motion for the populations of g and 1 read

$$\dot{\rho}_{11} = -\Gamma_h[(n_h+1)\rho_{11} - n_h\rho_{gg}], \quad \dot{\rho}_{gg} + \dot{\rho}_{11} = 0, \tag{5}$$

which yields the time-dependent solution

$$\rho^{th}_{11}(t) = \mathcal{N}_{th} n_h (1 - e^{-\Gamma_h(2n_h+1)t}), \quad \rho^{th}_{gg} + \rho^{th}_{11} = 1, \tag{6}$$

where superscript "th" indicates the thermal bath and the normalization $\mathcal{N}_{th} = [1 + 2n_h]^{-1}$. Following the approach outlined in Ref. [37], the population of level 1 excited by a coherent drive is given in Eq. (4) and $\rho_{gg}(t)$ is obtained using the population conservation $\rho_{11}(t) + \rho_{gg}(t) = 1$. This coherently excited populations 1 and g match with the thermal bath driven populations 1 and g given in Eq. (6). By matching the two we obtain n_h and Γ_h, that must satisfy

$$n_h = \frac{16\,\Omega_p^4\,(n_2+1)\delta^4}{(2n_2+1)\big(\delta^2+4\sigma_p^2\big)^4 - 32\,\Omega_p^4\,(n_2+1)\,\delta^4},$$
$$\Gamma_h = \Gamma_2 \frac{(2n_2+1)\big(\delta^2+4\sigma_p^2\big) - 32\,\sigma_p^4(n_2+1)\delta^4}{\big(\delta^2+4\,\sigma_p^2\big)^4}, \tag{7}$$

where we set $\omega_{2e'} \simeq \omega_{e'g}$. The effective thermal bath parameters defined in Eq. (7) yield the quantitative population match between the coherent and the thermal baths shown in Fig. 3(a). The agreement between the populations shown in Fig. 3(b) ensures the qualitative formation of an effective bath.

III. QUANTUM HEAT ENGINE

We next obtain the power and the efficiency, given by [47]

$$P = i\lambda(\omega_c - \omega_h)(\rho_{01} - \rho_{10}),$$
$$\dot{Q}_h = i\omega_h\lambda(\rho_{01} - \rho_{10}),$$
$$\eta = 1 - \frac{\omega_c}{\omega_h}. \tag{8}$$

where $\omega_h = \omega_1 - \omega_g$ and $\omega_c = \omega_0 - \omega_g$; n_h, n_c and Γ_h, Γ_c are the average occupation numbers and dephasing rates for the hot and cold baths, respectively. To find the steady state solution for ϱ_{01} and ϱ_{10} in Eq. (8), we follow the standard procedure for the three-level molecule given in the Supplemental Material of Refs. [28,37]. The output power and efficiency for the three-level QHE then read

$$P = \frac{2}{3}\frac{\lambda^2\Gamma_h\Gamma_c(n_c - n_h)(\omega_c - \omega_h)}{(\Gamma_h n_h + \Gamma_c n_c)(\lambda^2 + \Gamma_h\Gamma_c n_c n_h)},$$
$$\eta = 1 - \frac{1}{c_p - c_{21}}, \tag{9}$$

where $c_p = \omega_p/\omega_c$ and $c_{21} = \omega_{21}/\omega_c$.

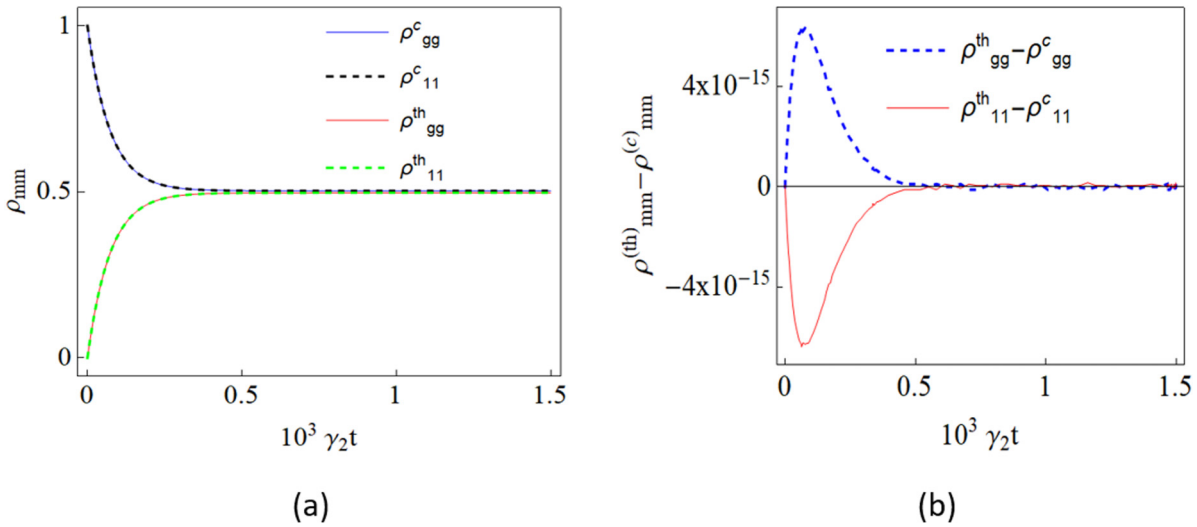

FIG. 3. (a) The population of ground state g and lowest excited state 1 obtained using the coherent bath in Eq. (4) (solid lines) and the thermal bath in Eq. (6) (dot-dashed) using parameters in Eq. (7). (b) The difference between populations of coherent and thermal baths $\rho_c - \rho_{th}$ for parameters in Eq. (7). The parameters read $n_2 = n_c = 100$, $\Gamma_2 = \Gamma_c = 0.002$ ps^{-1}, $\Omega_p = 0.0078$ eV, and $\sigma_p = 30.34$ cm^{-1}.

A. Classical two-photon pump

We now recast the output power in Eq. (9) using Eq. (7) in the high temperature limit where $n_c = n_1 \simeq T_c/\omega_c$, $n_2 = n_h \simeq T_2/\omega_{21}$, and $\omega_c = \omega_{0g}$. We then introduce an effective temperature of the hot bath $T_h = (\Omega_p\,\Gamma_2^2\ /2\,\delta)^{1/2}$ and the dimensionless temperature scale $\tau = T_c/T_h$. The pump energy scale $c_p = \omega_p/\omega_c$, the coupling scale $\lambda' = \lambda(\Gamma_2 T_c)^{-1/2}$, and the pump pulse width scale $\sigma_p' = \sigma_p^e\,\Gamma_2/\delta T_c$, where $\sigma_p^e = (\sigma_p^2 - \delta^2/4)^{1/2}$. Equation (9) for the dimensionless parameters given in Eq. (A22) can be finally maximized with respect to dimensionless variable c_{21} which yields

$$P_C^{\max} = \frac{4uv\lambda'\tilde{\tau}\left[2\,\mathcal{A} + 2\,\alpha u\,v + \tau^8\sigma_p'^8 c_p'(mu+v)\right]}{3\tau^8\sigma_p'^8(v-u\lambda')^2}, \qquad (10)$$

where $\mathcal{A} = \sqrt{u\,v\,(\tau^8\,c_p'\,\sigma_p'^8\ + \alpha\,u)(\tau^8\,c_p'\,\lambda'\,\sigma_p'^8 + \alpha v)}$, $\tilde{\tau} = 1 - \tau^8\sigma_p'^8$, and $c_p' = c_p - 1$. The efficiency corresponding to the maximum output power defined in Eq. (10) is given by

$$\eta_C^* = 1 - \frac{1}{c_p + \frac{\tilde{\tau}\sqrt{uv\left(c_p'\tau^8\sigma_p'^8+\alpha u\right)\left(\tau^8\lambda' c_p'\sigma_p'^8+\alpha v\right)}+uv\,\tilde{\tau}\alpha^2}{\tilde{\tau}\,\tau^8\sigma_p'^8\left[\alpha v+\lambda'\left(c_p'\tau^8\sigma_p'^8+\alpha u\right)\right]}}, \qquad (11)$$

where subscript C specifies the efficiency of the two-photon pump. We next assume the weak dissipation regime, i.e., $\omega_c \gg \Gamma_c$, which yields

$$\eta_{CW}^* = 1 - \frac{1}{c_p + \frac{\alpha^2 uv}{\tau^8\sigma_p'^8\left[\tau^8(c_p-1)\lambda'\sigma_p'^8+\alpha u\lambda'\right]}}, \qquad (12)$$

where subscript CW indicates the classical efficiency in the weak coupling regime. The entire parameter space corresponding to the efficiency given by Eq. (12) can be separated into four regions summarized in Table I and represented by the colorful two-dimensional (2D) shapes in Fig. 4(a). We use the dimensionless pump frequency c_p as a control parameter that depends on the effective temperature ratio τ; the pump pulse bandwidth $\sigma_p'^C$ (the classical pump bandwidth of σ_p') that depends on the dimensionless probe coupling field λ'; and τ, u, v, and α. We define the characteristic efficiency values describing the boundaries between the four regions corresponding to 0, $\eta_C/2$ (between I and II regions), $\eta_C/(2-\eta_C)$ (between III and IV), Carnot efficiency $\eta_C = 1-\tau$ (upper bound of IV), and Curzon-Ahlborn (CA) limit [48] $\eta_{CA} = 1 - \tau^{1/2}$ (between II and III). Note, that the two parameters of the pump field, the frequency ω_p and the Rabi frequency Ω_p, which define an effective hot bath temperature T_h and the pump bandwidth $\sigma_p'^C$, can be controlled experimentally. Thus the 2D parameter space $\{\tau, c_p\}$ and $\{\tau, \sigma_p'^C\}$ shows a constrained relation between the two as seen in Figs. 4(b) and 4(c), respectively.

We now compare the two-classical-photon pump with our previous work [37] where a single resonant pump has been taken to drive transition g–2. Let us highlight some important points here. First, the range of the pump frequency in the single photon case is $\omega_p \geqslant 2\omega_c$ while in the two photon case $\omega_p \geqslant \omega_c$, which affirms that the size of the system can be

TABLE I. Parameters of the coherent bath corresponding to the QHE efficiency bounds shown in Fig. 4, where $\xi = \frac{\alpha}{2(1-\eta_C)^8}$.

Bound	η_{CW}^*	c_p	$\sigma_p'^C$
I	0	1	$\sqrt[8]{\xi(u-\sqrt{u^2-\frac{4uv}{\lambda'}})}$
I/II	$\frac{\eta_C}{2}$	$\frac{2}{2-\eta_C}$	$\sqrt[8]{\xi(u-\sqrt{u^2-\frac{2uv(2-\eta_C)}{\lambda'}})}$
II/III	η_{CA}	$\frac{1}{\sqrt{1-\eta_C}}$	$\sqrt[8]{\xi(u-\sqrt{u^2-\frac{4uv\sqrt{1-\eta_C}}{\lambda'}})}$
III/IV	$\frac{\eta_C}{2-\eta_C}$	$\frac{2-\eta_C}{2(1-\eta_C)}$	$\sqrt[8]{\xi(u-\sqrt{u^2-\frac{8uv(1-\eta_C)}{(2-\eta_C)\lambda'}})}$
IV	η_C	$\frac{2}{1-\eta_C}$	$\sqrt[8]{\xi(u-\sqrt{u^2-\frac{4uv(1-\eta_C)}{\lambda'}})}$

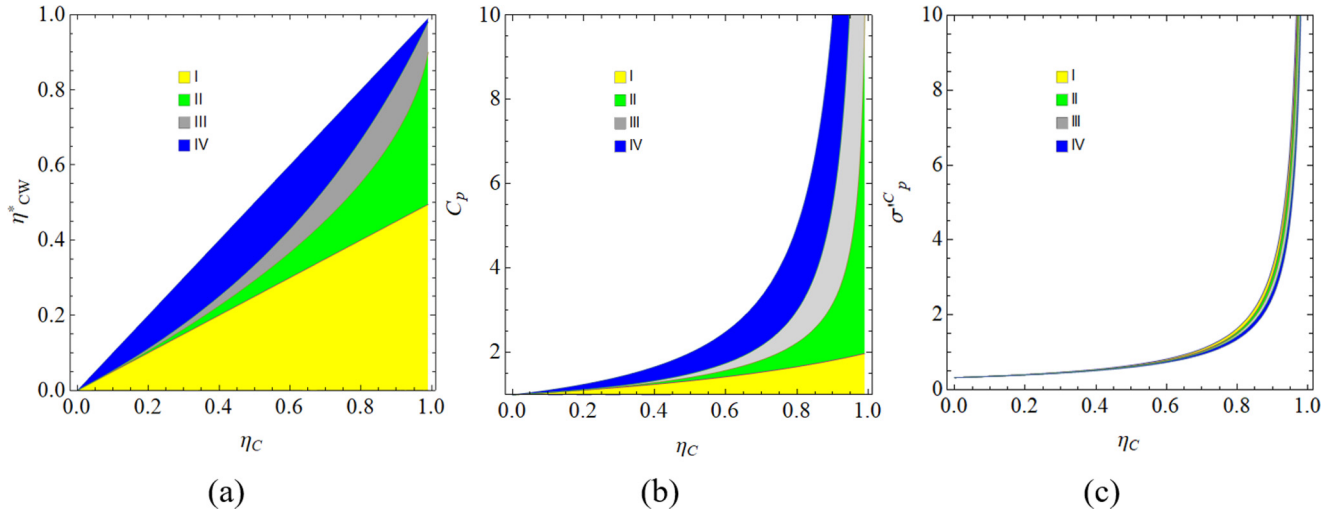

FIG. 4. (a) 2D mapping of the efficiency at maximum power η^*_{CW} in Eq. (12) vs Carnot efficiency $\eta_C = 1 - \tau$. (b) 2D mapping of the c_p vs η_C corresponding to (a). (c) 2D mapping of the σ'^C_p vs η_C corresponding to (a).

smaller. Second, this particular boundary is reached at different pump parameters. For instance, a CA limit is obtained for the single-photon pump at $c_p \simeq 2/\sqrt{\tau}$ and for the two photons $c_p \simeq 1/\sqrt{\tau}$, and its corresponding Rabi frequency is $\Omega_p^{CA} \simeq (4\omega_p/\omega_c)^4 T_c^2 \delta/\Gamma_2^2$. The factor of 2, which appears in the other bounds as well, originates from the quadratic scaling of the photon absorption probability with the input intensity for classical light.

B. Entangled two-photon pump

We now consider the case when the two photons driving transitions $g - e$ and $e - 2$ are entangled. A classical pump beam at frequency ω_p directed into a crystal is down converted into an entangled photon pair: signal (s) and idler (i) with frequencies ω_s and ω_i, respectively, as shown in Fig. 5(a). We consider type-II down conversion, which corresponds to orthogonally polarized signal and idler beams; this allows us to introduce the entanglement time and avoid complications with the selection rules. The different group velocities along two polarization axes create a time delay between the signal and the idler photons represented by entanglement time T. Owing to energy conservation, $\omega_p = \omega_i + \omega_s$. The photon pair is fully characterized by the twin photon state amplitude $\varphi(\omega_i, \omega_s) = \mathcal{A}(\omega_i + \omega_s)\Phi(\omega_i, \omega_s)$, where $\mathcal{A}(\omega) = \frac{A_0}{\omega - \omega_p + i\sigma}$ is a Lorentzian envelope function of the pump photon with bandwidth σ centered around ω_p and $\Phi(\omega_i, \omega_s) = \mathrm{sinc}[(\omega_s - \omega_i)T/2]$, originating from the phase matching inside the crystal (see Appendix B). The leading contribution to the population of state 2 calculated perturbatively according to the ladder diagram in Fig. 2, and by following the same approach given in Appendix A to obtain Eq. (4), and assuming that transition energy ω_{21} is much larger than dephasing rate Γ_2, the final populations read

$$\varrho_{11}(t) = \frac{\mathbb{N}^2\,\Gamma_2\,\tilde{n}_2\,\omega_{2e'}\,\omega_{e'g}\,\tilde{\omega}_{2g}^2(1 - e^{-\Gamma_2(2n_2+1)t})\theta}{\Gamma_2(2n_2+1)\left(\sigma_p^2 + \tilde{\omega}_{2g}^2\right)^2}, \qquad (13)$$
$$\varrho_{gg}(t) = 1 - \varrho_{11}(t),$$

where $\tilde{n}_2 = n_2 + 1$, $\tilde{\omega}_{2g} = \omega_{2g} - \omega_p$, $\theta = \mathrm{sinc}^2[\frac{T(\omega_{2e'} - \omega_{e'g})}{2}]$, and $\mathbb{N}^2 = \frac{\mathcal{N}^2 A_0^2 \mu_{eg}\mu_{e'e}\mu_{2e'}\mu_{21}}{4\epsilon_0^2 V^2}$ is a normalization. Assume for brevity that the normalization $\mathbb{N}$ of a quantum state is the same as that of a classical state [49], $\mathbb{N} = \Omega_{1'}\Omega_{2'}$. This ensures that all the dimensionless parameters for the entangled case are the same as in the classical one. Similarly to the classical case we now introduce an effective hot bath characterized by the thermal photon occupation number n_h and dephasing rate Γ_h which drives the transition $g - 1$, where the parameters of the bath are given by

$$n_h = \frac{\tilde{n}_2\,\theta\,\omega_{2e'}\omega_{ge'}\,\Omega_{1'}^2\Omega_{2'}^2\Delta^2}{(2n_2+1)\tilde{\Delta}^4 - 2\Omega_{1'}^2\Omega_{2'}^2\Delta^2\tilde{n}_2\omega_{2e'}\omega_{ge'}\theta},$$
$$\Gamma_h = \frac{\Gamma_2\left[(2n_2+1)\tilde{\Delta}^4 - 2\,\tilde{n}_2\,\theta\,\omega_{2e'}\omega_{ge'}\Omega_{1'}^2\Omega_{2'}^2\Delta^2\right]}{\tilde{\Delta}^4}, \qquad (14)$$

where $\tilde{\Delta}^2 = \Delta^2 + \sigma_p^2$ and $\Delta = \omega_{2g} - \omega_p$. Using the effective bath introduced for the system excited by the two entangled photons in Eq. (14), we can perfectly match the populations of

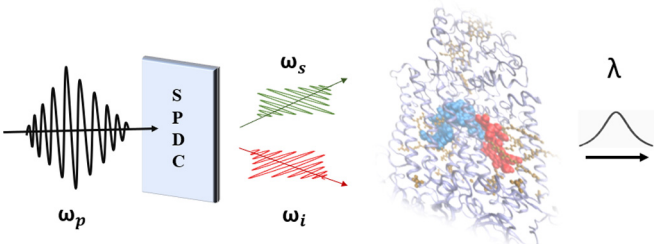

FIG. 5. (a) The pump photon frequency ω_p is down converted into two signal and idler photons with frequencies ω_s and ω_i, respectively. We consider spontaneous down conversion (SPDC) with energy conservation $\omega_p = \omega_i + \omega_s$. The entangled photons drive transitions $g \to e'$ and $e' \to 2$ and the probe field then stimulates the emission fromstate 1 to the excited vibrational level 0 of the ground electronic state.

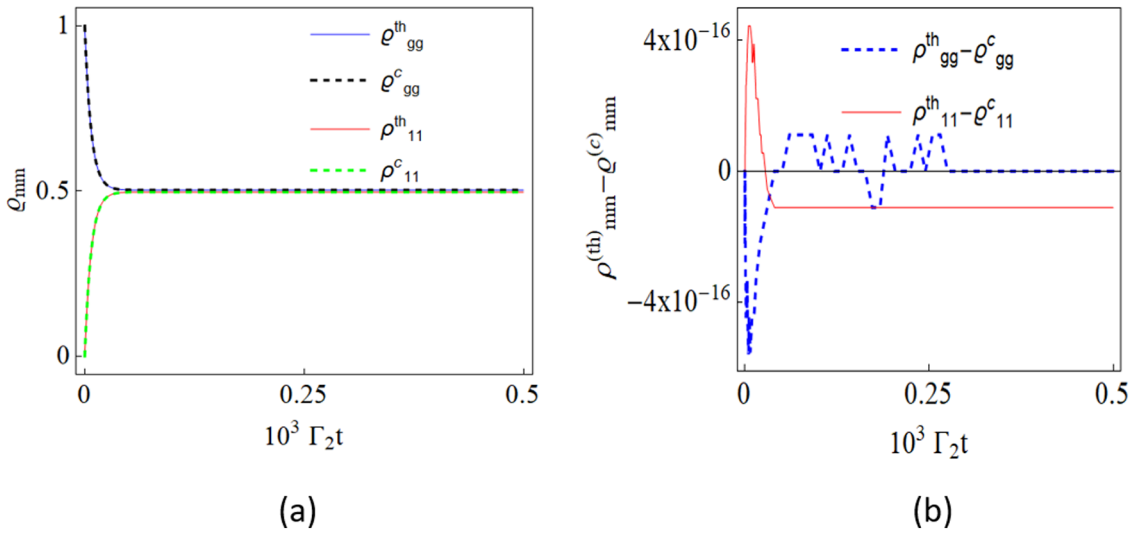

FIG. 6. (a) The population of ground state g and lowest excited state 1 obtained using a coherent bath in Eq. (13) and a thermal bath ρ_{th} using parameters in Eq. (14). (b) The difference between populations of coherent and thermal baths $\varrho_c - \rho_{th}$ for parameters in Eq. (14).

g and 1 driven by the thermal bath given in Eq. (6), as shown in Fig. 6. In the two-photon entangled, pump bandwidth scale $\sigma_p'^{Q} = \sigma_p^e \Gamma_2 / T_c \Delta$, where $\sigma_p^e = (\sigma_p^2 - \Delta^2)^{1/2}$.

Following the general approach outlined in Ref. [37] we apply the high temperature limit for the phonon bath, i.e., $T_2 \gg \omega_{21}$, and the maximum power with respect to (w.r.t.) c_{21}, which is recast in terms of dimensionless parameters given in Eq. (B16), yields

$$P_Q^{\max} = \frac{4uv\lambda' \mathcal{W} \tau^4 c_p'^2 \left(\sigma_p'^{Q}\right)^4 \left(\theta - \tau^4 \sigma_p'^4\right)}{3\theta \left(\mathcal{X} + \tau^4 v\, c_p' \left(\sigma_p'^{Q}\right)^4\right)\left(\mathcal{X} + \tau^4 u c_p' \lambda' \left(\sigma_p'^{Q}\right)^4\right)}, \tag{15}$$

where $\mathcal{X} = \mathcal{W} + \mathcal{E}$, $\mathcal{E} = \alpha\, u\, v\, \mathrm{sinc}^2[T(\omega_{2e'} - \omega_{ge'})/2]$, $\mathcal{W} = \sqrt{uv(\tau^4 c_p' \sigma_p'^4 + \mathcal{E}/v)(\tau^4 c_p' \lambda' \sigma_p'^4 + \mathcal{E}/u)}$, and $c_p' = c_p - 1$. The corresponding efficiency at maximum power is given by

$$\eta_Q^* = 1 - \frac{1}{c_p - \frac{(c_p - 1)\mathcal{E}}{\mathcal{W} + \mathcal{E}}}, \tag{16}$$

where subscript Q denotes the two-photon entangled pump. Similarly, in the weakly dissipating regime Eq. (16) can be recast as

$$\eta_{QW}^* = 1 - \frac{1}{c_p + \frac{u\, v\, \alpha^2\, \theta^2}{\tau^4 \lambda' \sigma_p'^4 [\alpha\, u\, \theta + (c_p - 1)\tau^4 \sigma_p'^4]}}, \tag{17}$$

where subscript QW specifies the weak dissipation limit of a two-photon entangled (quantum) pump and $\theta = \mathrm{sinc}^2[T(\omega_{2e'} - \omega_{ge'})/2]$. Similarly to the classical efficiency given in Eq. (12), the entire parameter space of the respective quantum efficiency in Eq. (17) is also divided into four regions, summarized in Table II. By comparing Tables I and II, it is clear that the four regions for η_{CW}^* and η_{QW}^* are identical when $\sigma_p'^{C} = \sigma_p'^{Q}$. The distinction between $\sigma_p'^{C}$ and $\sigma_p'^{Q}$ originates due to additional parameter T and the different pump intensity scalings (quadratic vs linear) [43] as mentioned in Tables I and II. The effective bandwidths for the two-classical-photon and two-entangled-photon pumps vs η_C are depicted in Figs. 7(a) and 7(b), respectively. Furthermore, the efficiency corresponding to the maximum output power for the quantum light is more robust than that for the classical light for a moderate range of τ as shown in Fig. 7(c), which will be discussed in the next subsection.

C. Maximum QHE power for the quantum and classical two-photon pumps

After maximization of QHE power with respect to the temperature and pump bandwidth we obtain different scalings for the classical and the entangled two-photon pumps [50]. Figure 8(a) shows numerically that in a specific temperature range the maximum output power in the entangled case can be larger than that in the classical case. The quantum enhancement for the maximum output power occurs for small τ. In this case Eqs. (10) and (15) yield,

TABLE II. The efficiency and pump scale are same as in Table I. The pump bandwidth parameters of the quantum bath corresponding to the QHE efficiency bounds in this table are shown in Fig. 7, where $\Xi = \frac{\alpha}{2(1-\eta_C)^4} \mathrm{sinc}^2[\frac{T(\omega_{2e'} - \omega_{ge'})}{2}]$.

Bound	η_{QW}^*	c_p	$\sigma_p'^{Q}$
I	0	1	$\sqrt[4]{\Xi(u - \sqrt{\frac{u(u\lambda' - 4v)}{\lambda'}})}$
I/II	$\frac{\eta_C}{2}$	$\frac{2}{2-\eta_C}$	$\sqrt[4]{\Xi(u - \sqrt{\frac{u[\lambda' u - 2v(2-\eta_C)]}{\lambda'}})}$
II/III	η_{CA}	$\frac{1}{\sqrt{1-\eta_C}}$	$\sqrt[4]{\Xi(u - \sqrt{\frac{u(u\lambda' - 4v\sqrt{1-\eta_C})}{\lambda'}})}$
III/IV	$\frac{\eta_C}{2-\eta_C}$	$\frac{2-\eta_C}{2(1-\eta_C)}$	$\sqrt[4]{\Xi(u - \sqrt{\frac{u[u(2-\eta_C)\lambda' - 8v(1-\eta_C)]}{(2-\eta_C)\lambda'}})}$
IV	η_C	$\frac{2}{1-\eta_C}$	$\sqrt[4]{\Xi(u - \sqrt{\frac{u[u\lambda' - 4v(1-\eta_C)]}{\lambda'}})}$

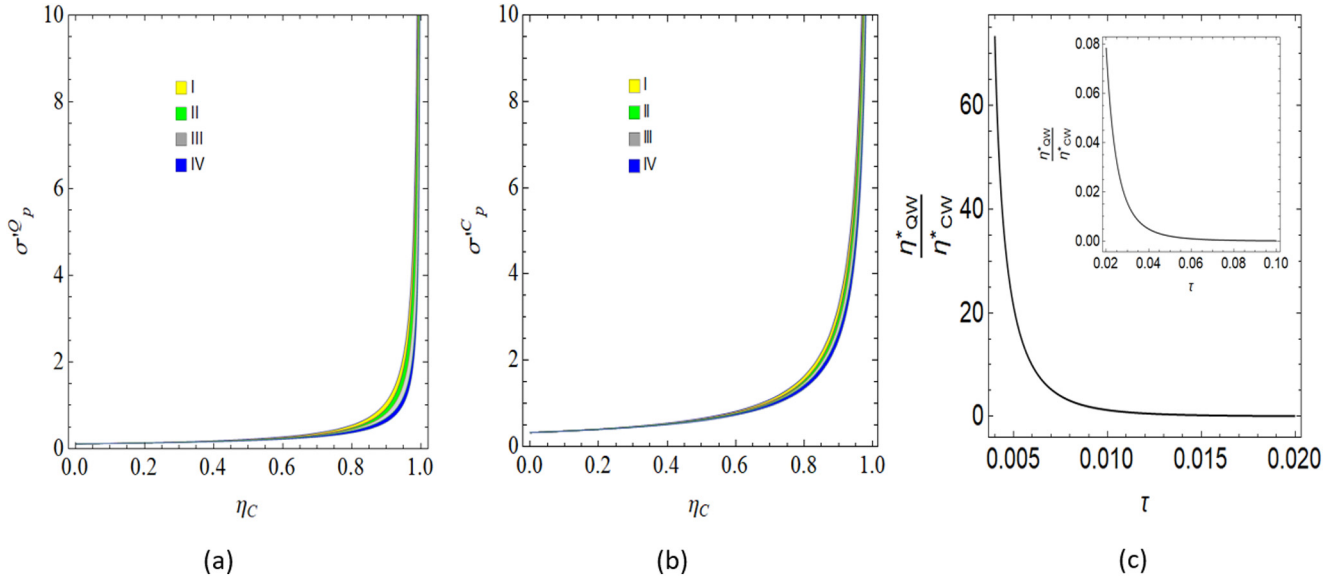

FIG. 7. (a) The 2D mapping of $\sigma_p'^{Q}$ vs η_C for entangled photons given in Table. II. (b) The 2D mapping of $\sigma_p'^{C}$ vs η_C of two pump photons from Table I. (c) The ratio of efficiency at maximum power in Eqs. (17) and (12) vs τ for $\mathrm{sinc}^2[\frac{T(\omega_{2e'}-\omega_{ge'})}{2}] \sim 1$ and $\eta^*_{QW} > \eta^*_{CW}$ occurs for small τ and also (in the inset) $\eta^*_{QW} < \eta^*_{CW}$ for considerably large value of τ. The parameters read $T_2 = T_c = 300$ K, $\omega_p = 1.3$ eV, $\omega_c = 0.012$ eV, $\Omega_p = 0.023$ eV, $\lambda = 0.1$ eV, $\delta = 0.00003$ eV, $\sigma_p = 200\ \mathrm{cm}^{-1}$, $\Gamma_2 = 0.71\ \mathrm{ps}^{-1}$, and $\Gamma_c = 0.025\ \mathrm{ps}^{-1}$.

respectively,

$$P_C^{\max} = \frac{\tau^8 (c_p - 1)^2 \lambda' (\sigma_p'^{c})^8}{3\,\alpha}, \tag{18}$$

$$P_Q^{\max} = \frac{\tau^4 (c_p - 1)^2 \lambda' \left(\sigma_p'^{Q}\right)^4}{3\,\alpha\,\mathrm{sinc}^2\left[\frac{T(\omega_{2e'}-\omega_{ge'})}{2}\right]}, \tag{19}$$

where for brevity $\sigma_p'^{C} = \sigma_p'^{Q} = \sigma_p'$, and from Eqs. (18) and (19) results we have $P_Q^{\max}/P_C^{\max} = \tau^{-4}\sigma_p'^{-4}\,\mathrm{sinc}^{-2}[T(\omega_{2e'} - \omega_{ge'})/2]$, which gives $P_Q^{\max} > P_C^{\max}$ for $\mathrm{sinc}^2[T(\omega_{2e'} - \omega_{ge'})/2] \simeq 1$ and $\sigma_p'\tau < 1$. The above analysis clearly indicates the relation between the effective bath temperature, the entanglement time, and the spectral bandwidth of the optical fields as well as the system energy scale and its effect on the optical measurements with the entangled light in open quantum systems. For instance in the limit of short entanglement time we can achieve quantum enhancement even in a highly anharmonic system as long as $|\omega_{2e'} - \omega_{e'g}| \ll 1/T$. Similarly, for the long entanglement time the quantum enhancement can

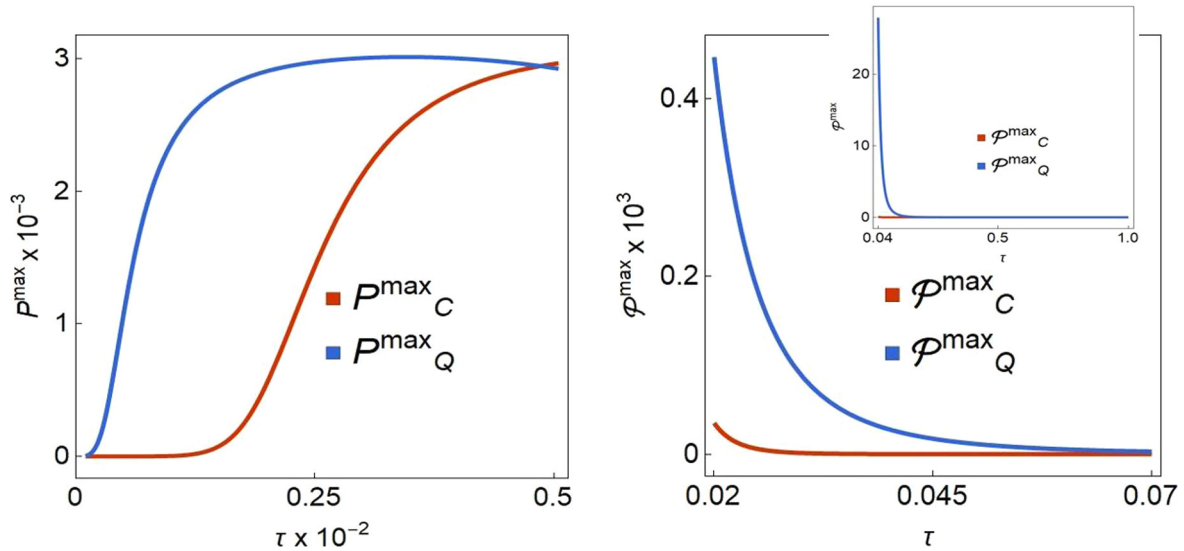

FIG. 8. (a) The numerical simulation of maximum QHE power vs τ showing the quantum advantage within a small range of τ. (b) Same as (a) for the spectroscopic power, showing the quantum advantage for the different regime of temperature scale. The vertical axes of (a) and (b) correspond to the maximum classical and quantum output power of the nonperturbed and perturbed regimes, respectively, and in this simulation the quantum advantages differ in their magnitude. The parameters are $T_2 = T_c = 300$ K, $\omega_p = 1.3$ eV, $\omega_c = 0.012$ eV, $\Omega_p = 0.023$ eV, $\lambda = 0.1$ eV, $\delta = 0.00003$ eV, $\sigma_p = 200\ \mathrm{cm}^{-1}$, $\Gamma_2 = 0.71\ \mathrm{ps}^{-1}$, and $\Gamma_c = 0.025\ \mathrm{ps}^{-1}$.

be reached for a nearly harmonic system ($\omega_{2e'} \simeq \omega_{e'g}$). In the same time inequality $\sigma'_p\tau < 1$ yields an additional requirement for the pumping source such that $\Omega_p > 4\delta(\sigma^e_p)^2/\Delta^2$.

IV. SPECTROSCOPIC REGIME

So far we have discussed QHE regime in which the density matrix has been solved nonperturbatively. We now focus on the pump-probe spectroscopic signal derived by the perturbative approach in the light-matter interaction. Reference [37] shows the apparent connection between the thermodynamics of the QHE and the spectroscopy that emerges as an incoherent control tool for the optimization of optical measurements, which can enhance the yield of fluorescence and pump-probe measurements and improve the signal-to-noise ratio in a wide class of the optical signals. Here we explore the class of two-photon pump classical probe signals using classical and entangled two-photon pumps. To that end the coherence ρ_{01} and ρ_{10} which enter in the definition of Eq. (8) can be calculated perturbatively.

Using Eq. (A21) (in Appendix A), while keeping the leading order terms following the Feynman diagram in Fig. 2, we substitute the solution for the population $\rho_{11}(t)$ from Eq. (4) and solve for $\rho_{01}(t)$ for the two-photon pump, which yields

$$\rho_{01} = -\frac{32\, i\, \Gamma_2\, \lambda\, n_2\, \delta^4\, {\Omega^4}_p}{\left(\delta^2 + 4\sigma_p^2\right)^4 \sigma_{\rm pr}(\Gamma_c n_c + \Gamma_2 n_2)(5\Gamma_2 n_2 + \Gamma_c n_c)},$$
$$\rho_{10} = -\rho_{01}. \tag{20}$$

Similarly, to obtain the coherence $\varrho_{01}(t)$ while keeping the leading order terms following the Feynman diagram in Fig. 2, we substitute the solution for the population $\varrho_{11}(t)$ from Eq. (13) and we get

$$\varrho_{01} = -\frac{2\, i\, \Gamma_2\, \lambda\, n_2\, \delta^4\, {\Omega^2}_{1'} {\Omega^2}_{2'} {\rm Sinc}^2\left[\frac{T(\omega_{2e'} - \omega_{ge'})}{2}\right]}{\left(\Delta^2 + \sigma_p^2\right)^4 \sigma_{\rm pr}(\Gamma_c n_c + \Gamma_2 n_2)(5\Gamma_2 n_2 + \Gamma_c n_c)},$$
$$\varrho_{10} = -\varrho_{01}. \tag{21}$$

Utilizing Eq. (20) we obtain the power for the classical two-photon pump in Appendix C, Eq. (C1). After optimizing w.r.t. c_{21}, the maximum power yields

$$\mathcal{P}_C^{\rm max} = \frac{u\lambda'(3c_p + 5\alpha u - 3 - \mathcal{C})}{2\tau^8 \sigma_{\rm pr} \sigma'^8_p}, \tag{22}$$

where $\mathcal{C} = \sqrt{5(c_p + \alpha u - 1)(c_p + 5\alpha u - 1)}$. Similarly, we optimize the power for the entangled two-photon pump in Eq. (C2) and its maximum yields

$$\mathcal{P}_Q^{\rm max} = \frac{4\alpha c_{21} u^2 (c_p - c_{21} - 1)\lambda' {\rm sinc}^2\left[\frac{T(\omega_{2e'} - \omega_{ge'})}{2}\right]}{\tau^4 \sigma_{\rm pr}(c_{21} + \alpha u)(c_{21} + 5\alpha u){\sigma'^4}_p}. \tag{23}$$

In Appendix C, we demonstrate numerically that the maximum power for the quantum light is much larger than that for the classical light for a moderate range of $\tau < 1$ in Eqs. (23) and (22) [see Fig. 8(b)]. The ratio of maximum power for the corresponding equations reads

$$\frac{\mathcal{P}_Q^{\rm max}}{\mathcal{P}_C^{\rm max}} = \tau^4 \sigma'^4_p {\rm sinc}^2\left[\frac{T(\omega_{2e'} - \omega_{ge'})}{2}\right]. \tag{24}$$

For the short entanglement time ${\rm sinc}^2[\frac{T(\omega_{2e'} - \omega_{ge'})}{2}] \simeq 1$ and in the limit of $\sigma'_p\tau > 1$ we obtain $\mathcal{P}_Q^{\rm max} > \mathcal{P}_C^{\rm max}$. We therefore have identified the parameter regime where maximum power for the entangled two-photon pump is enhanced compared to the classical case using the perturbative regime. In comparison to the QHE (nonperturbative) regime the power increase due to the entanglement in the spectroscopic (perturbative) regime occurs when the bath temperature ratio is $\tau > 1/\sigma'_p$, whereas in the former case $\tau < 1/\sigma'_p$, which agrees with the strong pump (nonperturbative) vs weak pump (perturbative) limits taken in these two cases.

Simulations of the maximum power for the QHE regime given in Eqs. (18) and (19) and for the spectroscopic regime given in Eqs. (22) and (23) are shown in Fig. 8 (Appendix C). It shows that the quantum enhancement of power is achieved at different timescales: in the QHE regime at $0 < \tau < 0.5 \times 10^{-2}$ and in spectroscopic regime at $0 < \tau < 0.07$.

V. SUMMARY

It has been shown that the two-photon absorption of entangled light may enhance the Raman excitation [51] due to different intensity scalings at low photon fluxes. In the present analysis the two-photon absorption in the open quantum system regime benefits from additional control parameters using an incoherent control scheme by mimicking QHEs. In this proposed model we analytically explored the characteristics of two-photon absorptions for classical and entangled pair of photons and their dependence on additional degrees of freedom, due to which we get the maximum work, in both the weak and strong intensity approximations. By using the approach of [37] we developed a connection between the thermodynamics of the QHE and the spectroscopy. The transfer of entanglement to the system allows one to optimize the detailed balance in system-bath driven optical transitions in an open quantum system allowing a QHE to operate near the thermodynamic cycle, which consequently provides an enhanced yield of conversion between the pump and the probe fields. Our results can be further extended to Raman, hyper-Raman, and other techniques that require additional control over illumination intensity and pump light statistics.

ACKNOWLEDGMENTS

We gratefully acknowledge support from the National Science Foundation of China (No. 11934011), the Zijiang Endowed Young Scholar Fund, the East China Normal University, and the Overseas Expertise Introduction Project for Discipline Innovation (111 Project, B12024). M.Q. acknowledges support from CSC Scholarship (CSC No. 2018 DFH 007778).

APPENDIX A: EFFECTIVE HEAT BATH

The master equation in Liouville space is

$$\frac{d\hat{\rho}}{dt} = -\frac{i}{\hbar}[\hat{H}_{\rm int}(t),\ \hat{\rho}], \tag{A1}$$

We define the superoperator in Liouville space by acting on a arbitrary operator X:

$$\hat{H}_{\text{int},-}\hat{X} = \hat{H}_{\text{int}}\hat{X} - \hat{X}\hat{H}_{\text{int}}. \tag{A2}$$

Now, the solution of Eq. (A1) can be written as a Dyson series in Liouville space. Hence, we obtain the density matrix

$$\hat{\rho}(t) = \mathcal{G}(t,t_0)\hat{\rho}(t_0), \tag{A3}$$

with the Liouville space Green's function

$$\mathcal{G}(t,t_0) = \hat{\mathcal{T}}\left[-\frac{i}{\hbar}\exp\int_{t_0}^{t}\hat{H}_{\text{int},-}(\tau)\right], \tag{A4}$$

where $\hat{\mathcal{T}}$ is a time ordering superoperator which is defined by

$$\hat{\mathcal{T}}\hat{A}(t_1)\hat{B}(t_2) \equiv \Theta(t_1-t_2)\hat{A}(t_1)\hat{B}(t_2) + \Theta(t_2-t_1)\hat{B}(t_2)\hat{A}(t_1), \tag{A5}$$

where $\hat{A}(t)$ and $\hat{B}(t)$ are two arbitrary superoperators and $\Theta(t)$ is the Heaviside function. A perturbative expansion of the Dyson series yielding the leading order contribution of Eq. (A3) reads

$$\rho_{11}(t) = \frac{1}{\hbar^4}\int_{t_0}^{t}d\tau_1\int_{t_0}^{\tau_1}d\tau_2\int_{t_0}^{t_2}d\tau_3\int_{t_0}^{\tau_3}d\tau_4\langle\langle\hat{H}_{\text{int},-}(\tau_1) \times \hat{H}_{\text{int},-}(\tau_2)\hat{H}_{\text{int},-}(\tau_3)\hat{H}_{\text{int},-}(\tau_4)\hat{\rho}(t_0)\rangle\rangle, \tag{A6}$$

where $\langle\langle\cdot\rangle\rangle = \text{Tr}[\cdot,\hat{\rho}(t)]$ represents the trace with the density operator. The population of the excited state due to relaxation 2–1 is represented by a diagrammatic Feynman ladder in Fig. 2 given by

$$\begin{aligned}\rho^a_{11}(t) &= \frac{1}{\hbar^4}\int^{t}d\tau_1\int^{\tau_1}d\tau_2\int^{\tau_2}d\tau_3\int^{\tau_3}d\tau_4\langle\langle\mathcal{G}_{11,22}(t-\tau_1)\\ &\times\hat{\mathcal{V}}_{2e}\mathcal{G}_{2e,2e}(\tau_1-\tau_2)\hat{\mathcal{V}}^{\dagger}_{2e}\mathcal{G}_{ee,e'e'}(\tau_2-\tau_3)\hat{\mathcal{V}}_{e'g}\\ &\times\mathcal{G}_{e'g,e'g}(\tau_3-\tau_4)\hat{\mathcal{V}}^{\dagger}_{e'g}\rangle\rangle\langle\hat{E}^{\dagger}_1(\tau_3)\hat{E}^{\dagger}_2(\tau_1)\hat{E}_2(\tau_2)\hat{E}_1(\tau_4)\rangle\\ &= \frac{1}{\hbar^4}\int^{t}dt_1\int^{t_1}dt_2\int^{t_2}dt_3\int^{t_3}dt_4\langle\langle\mathcal{G}_{11,22}(t_1)\\ &\times\hat{\mathcal{V}}_{2e}\mathcal{G}_{2e,2e}(t_2)\hat{\mathcal{V}}^{\dagger}_{2e}\mathcal{G}_{ee,e'e'}(t_3)\hat{\mathcal{V}}_{e'g}\mathcal{G}_{e'g,e'g}(t_4)\hat{\mathcal{V}}^{\dagger}_{e'g}\rangle\rangle\\ &\times\langle\hat{E}^{\dagger}_1(t-t_1-t_2-t_3)\hat{E}^{\dagger}_2(t-t_1)\hat{E}_2(t-t_1-t_2)\\ &\times\hat{E}_1(t-t_1-t_2-t_3-t_4)\rangle,\end{aligned} \tag{A7}$$

where $t_1 = t-\tau_1$, $t_2 = \tau_1-\tau_2$, $t_3 = \tau_2-\tau_3$, $t_4 = \tau_3-\tau_4$, and $\hat{\mathcal{V}}$ is a time independent dipole operator in Liouville space. Now, we transform the fields components in frequency domain, and it can be recast as

$$\begin{aligned}\rho^a_{11}(t) &= \frac{1}{\hbar^4}\int\frac{d\omega_1\,d\omega_{1'}\,d\omega_2\,d\omega_{2'}}{(2\pi)^4}\langle\hat{\Omega}^{\dagger}_1(\omega_{1'})\hat{\Omega}^{\dagger}_2(\omega_{2'})\hat{\Omega}_2(\omega_2)\hat{\Omega}_1(\omega_1)\rangle\int_{-\infty}^{\infty}dt_1dt_2dt_3dt_4\mathcal{G}_{11,22}(t_1)\mathcal{G}_{2e,2e}(t_2)\\ &\times\ \mathcal{G}_{ee,e'e'}(t_3)\mathcal{G}_{e'g,e'g}(t_4)e^{i\omega_{1'}(t-t_1-t_2-t_3)+i\omega_{2'}(t-t_1)-i\omega_2(t-t_1-t_2)-i\omega_1(t-t_1-t_2-t_3-t_4)}\\ &= \frac{1}{\hbar^4}\int\frac{d\omega_1\,d\omega_{1'}\,d\omega_2\,d\omega_{2'}}{(2\pi)^4}\langle\hat{\Omega}^{\dagger}_1(\omega_{1'})\hat{\Omega}^{\dagger}_{2'}(\omega_{2'})\hat{\Omega}_2(\omega_2)\hat{\Omega}_1(\omega_1)\rangle e^{i(\omega_{1'}+\omega_{2'}-\omega_1-\omega_2)t}\\ &\times\mathcal{G}_{11,22}(\omega_1+\omega_2-\omega_{2'}-\omega_{1'})\mathcal{G}_{2e,2e}(\omega_1+\omega_2-\omega_{1'})\mathcal{G}_{ee,e'e'}(\omega_1-\omega_{1'})\mathcal{G}_{e'g,e'g}(\omega_1),\end{aligned} \tag{A8}$$

where $\hat{\Omega}_1(\omega_1) = \mu_{ge}\sqrt{\frac{\hbar\omega_1}{2\mathbf{V}\epsilon_0}}\hat{a}_1(\omega_1)e^{-i\omega_1 t}$; we similarly define $\hat{\Omega}_2(\omega_2)$, $\hat{\Omega}^{\dagger}_1(\omega'_1)$, and $\hat{\Omega}^{\dagger}_2(\omega'_2)$.

The population Green's functions $\mathcal{G}_{11,22}$, $\mathcal{G}_{ee,e'e'}$, and $\mathcal{G}_{gg,00}$ originate from the solution of coupled transport (relaxation) equations:

$$\begin{aligned}\dot{\rho}_{22} &= -\Gamma_2(n_2+1)\rho_{22} + \Gamma_2 n_2\rho_{11},\\ \dot{\rho}_{11} &= \Gamma_2(n_2+1)\rho_{22} - \Gamma_2 n_2\rho_{11},\end{aligned} \tag{A9}$$

$$\begin{aligned}\dot{\rho}_{e'e'} &= -\Gamma_e(n_e+1)\rho_{e'e'} + \Gamma_e n_e\rho_{ee},\\ \dot{\rho}_{ee} &= \Gamma_e(n_e+1)\rho_{e'e'} - \Gamma_e n_e\rho_{ee},\end{aligned} \tag{A10}$$

$$\begin{aligned}\dot{\rho}_{00} &= -\Gamma_c(n_c+1)\rho_{00} + \Gamma_c n_c\rho_{gg},\\ \dot{\rho}_{gg} &= \Gamma_c(n_c+1)\rho_{00} - \Gamma_c n_c\rho_{gg}.\end{aligned} \tag{A11}$$

Equations (A9)–(A11) can be recast as a Pauli master equation:

$$\dot{\rho}_{ii}(t) = -\sum_{ii,jj}\kappa_{ii,jj}\rho_{jj}(t), \tag{A12}$$

where $\kappa_{ii,jj}$ is the population transport matrix. In Eq. (A12), the diagonal elements, $i=j$, $\kappa_{ii,ii}$ are positive, whereas the off-diagonal elements, $i\neq j$, $\kappa_{ii,jj}$ are negative. The population transport matrix satisfies the population conservation $\sum_i\kappa_{ii,jj} = 0$. The evolution of the diagonal elements is defined by the population Green function, $\rho_{jj}(t) = \sum_i\mathcal{G}_{jj,ii}(t)\rho_{ii}(0)$, where $\mathcal{G}_{jj,ii}(t)$ is given [52]

$$\mathcal{G}_{jj,ii}(t) = \sum_n\xi^{(R)}_{jn}D^{-1}_{nn}\exp(-\lambda_n t)\xi^{(L)}_{ni}, \tag{A13}$$

where λ_n is the nth eigenvalue of left and right eigenvectors $(\xi^{(L)}_n, \xi^{(R)}_n)$ and $D = \xi^L\xi_R$ is a diagonal matrix. Using Eq. (A13) we obtain for the population Green's functions

$$\mathcal{G}_{00,gg}(t) = \frac{n_c(1-e^{-t(1+2n_c)\Gamma_c})}{(1+2n_c)}, \tag{A14}$$

$$\mathcal{G}_{ee,e'e'}(t) = \frac{n_e(1-e^{-t(1+2n_e)\Gamma_e})}{(1+2n_e)}, \tag{A15}$$

$$\mathcal{G}_{11,22}(t) = \frac{(1+n_2)(1-e^{-t(1+2n_2)\Gamma_2})}{(1+2n_2)}. \tag{A16}$$

We use Eqs. (A14)–(A16) and Liouville space Green's functions $\mathcal{G}(\omega) = \frac{-(n_i+1)\Gamma_i}{(\omega+i\epsilon)[\omega+i(2n_i+1)\Gamma_i]}$, where n_i is the average phonon occupation number and Γ_i is the dephasing rate for the $i \leftrightarrow i-1$ transition. To examine field-induced fourth-order correlations of matter, we utilize the reduced density matrix obtained by tracing out the field degrees of freedom, Eq. (A8), as

$$\begin{aligned}\rho^a_{11}(t) = \frac{\Gamma_2\Gamma_e(n_2+1)(n_e+1)e^{-(\Gamma_{21}+\epsilon_2)t}}{(\epsilon_2-\Gamma_{21})(\epsilon_e-\Gamma_{ee'})}\Big\langle\Big(e^{\Gamma_{21}t}\big(\hat\Omega_1^\dagger[\,\omega_{e'g}+i(\epsilon_e-\Gamma_{e'g})]\hat\Omega_2^\dagger[\,\omega_{2e}+i(\epsilon_2-\Gamma_{2e})]\hat\Omega_2[\,\omega_{2e}+i(\epsilon_e-\Gamma_{2e})]\\ -\hat\Omega_1^\dagger[\,\omega_{e'g}+i(\Gamma_{ee'}-\Gamma_{e'g})]\hat\Omega_2^\dagger[\,\omega_{2e}+i(\epsilon_2-\Gamma_{2e})]\hat\Omega_2[\,\omega_{2e}-i(\Gamma_{2e}-\Gamma_{ee'})]\big)\\ +e^{\epsilon_2 t}\big(\hat\Omega_1^\dagger[\,\omega_{e'g}+i(\Gamma_{ee'}-\Gamma_{e'g})]\hat\Omega_2^\dagger[\,\omega_{2e}+i(\Gamma_{21}-\Gamma_{2e})]\hat\Omega_2[\,\omega_{2e}-i(\Gamma_{2e}-\Gamma_{ee'})]\\ -\hat\Omega_1^\dagger[\,\omega_{e'g}+i(\epsilon_e-\Gamma_{e'g})]\hat\Omega_2^\dagger[\,\omega_{2e}+i(\Gamma_{21}-\Gamma_{2e})]\hat\Omega_2[\,\omega_{2e}+i(\epsilon_e-\Gamma_{2e})]\big)\Big)\hat\Omega_1[\omega_{e'g}-i\Gamma_{ee'}]\Big\rangle,, \end{aligned} \tag{A17}$$

where ϵ_2 and ϵ_e are the dephasing rates at transitions 2–1 and e–e', respectively.

The populations of vibrational state 1 from Feynman diagrams (b) and (c) are

$$\begin{aligned}\rho^b_{11}(t) &= \frac{1}{\hbar^4}\int^t dt_1\int^{t_1}dt_2\int^{t_2}dt_3\int^{t_3}dt_4\langle\langle\mathcal{G}_{11,22}(t-t_1)\hat{\mathcal{V}}^\dagger_{2e}\mathcal{G}_{e2,e2}(t_1-t_2)\hat{\mathcal{V}}_{2e}\mathcal{G}_{ee,e'e'}(t_2-t_3)\\ &\times\hat{\mathcal{V}}_{e'g}\mathcal{G}_{e'g,e'g}(t_3-t_4)\hat{\mathcal{V}}^\dagger_{eg}\rangle\rangle\langle\hat E_1^\dagger(t_3)\hat E_2^\dagger(t_2)\hat E_2(t_1)\hat E_1(t_4)\rangle\\ &= \frac{\Gamma_2\Gamma_e(n_2+1)(n_e+1)e^{-(\Gamma_{21}+\epsilon_2)t}}{(\epsilon_2-\Gamma_{21})(\epsilon_e-\Gamma_{ee'})}\Big\langle\Big(e^{\Gamma_{21}t}\big(\hat\Omega_1^\dagger[\omega_{e'g}+i(\epsilon_e-\Gamma_{e'g})]\hat\Omega_2^\dagger[\omega_{2e}-i(\epsilon_e-\Gamma_{2e})]\hat\Omega_2[\omega_{2e}-i(\epsilon_2-\Gamma_{2e})]\\ &-\hat\Omega_1^\dagger[\omega_{e'g}-i(\Gamma_{e'g}-\Gamma_{ee'})]\hat\Omega_2^\dagger[\omega_{2e}-i(\Gamma_{ee'}-\Gamma_{2e})]\hat\Omega_2[\omega_{2e}-i(\epsilon_2-\Gamma_{2e})]\big)+e^{\epsilon_2 t}\big(\hat\Omega_1^\dagger[\omega_{e'g}-i(\Gamma_{e'g}-\Gamma_{ee'})]\\ &\times\hat\Omega_2^\dagger[\omega_{2e}-i(\Gamma_{ee'}-\Gamma_{2e})]\hat\Omega_2[\omega_{2e}-i(\Gamma_{21}-\Gamma_{2e})]-\hat\Omega_1^\dagger[\omega_{e'g}+i(\epsilon_e-\Gamma_{e'g})]\hat\Omega_2^\dagger[\omega_{2e}-i(\epsilon_e-\Gamma_{2e})]\\ &\times\hat\Omega_2[\omega_{2e}-i(\Gamma_{21}-\Gamma_{2e})]\big)\Big)\hat\Omega_1[\omega_{e'g}-i\Gamma_{e'g}]\Big\rangle. \end{aligned} \tag{A18}$$

$$\begin{aligned}\rho^c_{11}(t) &= \frac{1}{\hbar^4}\int^t dt_1\int^{t_1}dt_2\int^{t_2}dt_3\int^{t_3}dt_4\langle\langle\mathcal{G}_{11,22}(t-t_1)\hat{\mathcal{V}}_{2e'}\mathcal{G}_{2e',2e'}(t_1-t_2)\hat{\mathcal{V}}_{e'g}\mathcal{G}_{2g,2g}(t_2-t_3)\\ &\times\hat{\mathcal{V}}^\dagger_{2e'}\mathcal{G}_{e'g,e'g}(t_3-t_4)\hat{\mathcal{V}}^\dagger_{eg}\rangle\rangle\langle\hat E_1^\dagger(t_2)\hat E_2^\dagger(t_1)\hat E_2(t_3)\hat E_1(t_4)\rangle\\ &= \frac{\Gamma_e(n_e+1)e^{-(\Gamma_{21}+\epsilon_2)t}}{(\Gamma_{21}-\epsilon_2)}\Big\langle\hat\Omega_1^\dagger[\omega_{2g}-\omega_{2e'}+i(\Gamma_{2e'}-\Gamma_{2g})]\big(e^{\Gamma_{21}t}\hat\Omega_2^\dagger[\omega_{2e'}+i(\epsilon_2-\Gamma_{2e'})]\\ &-e^{\epsilon_2 t}\hat\Omega_2^\dagger[\omega_{2e'}+i(\Gamma_{21}-\Gamma_{2e'})]\big)\hat\Omega_2[\omega_{2g}-\omega_{e'g}+i(\Gamma_{e'g}-\Gamma_{2e})]\hat\Omega_1[\omega_{e'g}-i\Gamma_{e'g}]\Big\rangle. \end{aligned} \tag{A19}$$

The total population $\rho_{11}(t) = \mathrm{Re}(\rho^a_{11}+\rho^b_{11}+\rho^c_{11})$ induced by a pulse with Lorentzian shape is defined, e.g., $\hat\Omega_1[\omega_{e'g}+i\Gamma_{e'g}] = \frac{\hat\Omega_{1'}}{\omega_{e'g}-\omega_0+i\sigma_p-i\Gamma_{e'g}}$, where ω_0 is the central frequency and $\omega_{e'g}$ is the e'–g transition frequency. Employing the approximation $\Gamma_{21} = \Gamma_2(2n_2+1) \gg \epsilon_2$, assuming that the transition energy is much larger than the decay constant. The total population of level 1 by employing Eqs. (A17), (A18), and (A19) yields

$$\rho_{11}(t) = \frac{16(n_2+1)\,|\Omega_p|^4\tilde\omega^2_{2e'}\,\tilde\omega^2_{e'g}(1-e^{\Gamma_2(2n_2+1)t})}{(2n_2+1)\big(\sigma_p^2+\tilde\omega^2_{2e'}\big)^2\big(\sigma_p^2+\tilde\omega^2_{e'g}\big)^2}, \tag{A20}$$

where $\tilde\omega_{2e'} = \omega_{2e'}-\omega_0$, $\tilde\omega_{e'g} = \omega_{e'g}-\omega_0$, and we set $|\Omega_{1'}| = |\Omega_{2'}| = |\Omega_{1'}^\dagger| = |\Omega_{2'}^\dagger| = |\Omega_p|$.

We consider a three-level molecular system with the ground state g, single electronic excited state e, and double excited electronic state f shown in Fig. 1(a). We denote the vibrational states of electronic ground states 0 and g and vibrational double excited states of electronic states 2 and 1, and e and e' are single electronic states. The corresponding equation of motion for the density matrix is given by

$$\begin{aligned}\dot\rho_{gg}(t) &= i\Omega_1[\rho_{ge}(t)-\rho_{eg}(t)]+\Gamma_c(n_c+1)\rho_{00}(t)-\Gamma_c n_c\rho_{gg}(t),\\ \dot\rho_{ee}(t) &= -i\Omega_1[\rho_{ge}(t)-\rho_{eg}(t)]+i\Omega_2[\rho_{g2}(t)-\rho_{2e}(t)],\\ \dot\rho_{22}(t) &= -i\Omega_2(t)[\rho_{e2}(t)-\rho_{2e}(t)]-\Gamma_2(n_2+1)\rho_{22}(t)+\Gamma_2 n_2\rho_{11}(t),\\ \dot\rho_{11}(t) &= -i\lambda[\rho_{01}(t)-\rho_{10}(t)]-\Gamma_2(n_2+1)\rho_{00}(t)+\Gamma_c n_c\rho_{gg}(t),\end{aligned}$$

$$\dot{\rho}_{2e}(t) = i\Omega_2(t)[\rho_{22}(t) - \rho_{ee}(t)] + i\Omega_1\rho_{2g}(t) - \left\{\frac{\Gamma_2(n_2+1)}{2} + i(\omega_{2e} - \nu_2)\rho_{2e}\right\},$$

$$\dot{\rho}_{eg}(t) = i\Omega_1[\rho_{ee}(t) - \rho_{gg}(t)] - i\Omega_1\rho_{2g}(t) - \left\{\frac{\Gamma_c n_c}{2} + i(\omega_{eg} - \nu_1)\right\}\rho_{eg}(t),$$

$$\dot{\rho}_{2g}(t) = i\Omega_1\rho_{2e}(t) - i\Omega_2\rho_{eg}(t) - \left\{\frac{\Gamma_2(n_2+1)}{2} + \frac{\Gamma_c n_c}{2} + i(\omega_{2g} - \nu_1 - \nu_2)\right\}\rho_{2g}(t),$$

$$\dot{\rho}_{10}(t) = i\lambda[\rho_{11}(t) - \rho_{00}(t)] - \left\{\frac{\Gamma_2 n_2}{2} + \frac{\Gamma_c(n_c+1)}{2} + i(\omega_{10} - \nu_{pr})\right\}\rho_{10}(t),$$

$$\dot{\rho}_{e2}(t) = \dot{\rho}^{\dagger}_{2e}, \quad \dot{\rho}_{ge}(t) = \dot{\rho}^{\dagger}_{eg}, \quad \dot{\rho}_{g2}(t) = \dot{\rho}^{\dagger}_{2g}, \quad \dot{\rho}_{01}(t) = \dot{\rho}^{\dagger}_{10}, \tag{A21}$$

where $\Gamma_2/2$ is a dephasing rate and $n_2 = [\exp(\omega_{21}/T_c) - 1]^{-1}$ is the average phonon occupation number corresponding to $1-2$ at temperature T_2.

The output power in Eq. (9) using Eq. (7) in the high temperature limit becomes

$$P_C = \frac{4\,T_c\,\omega_c\,c_{21}\,\tau^8 u\,v\,\tilde{c}_p\lambda'\sigma_p'^8\left(\tilde{c}_{21} - \tau^8(\tilde{c}_{21} - c_{21})\sigma_p'^8\right)}{3\left(c_{21}\,\tau^8\,\sigma_p'^8 + u\,\tilde{c}_{21}\right)\left(c_{21}\tau^8\lambda'\sigma_p'^8 + v\tilde{c}_{21}\right)}, \tag{A22}$$

where subscript C specifies the two-photon pump and $\tilde{c}_p = (c_p - c_{21} - 1)$, $\tilde{c}_{21} = \alpha - c_{21}$, $u = \Gamma_2\omega_c/\Gamma_c T_c$, $v = \Gamma_c/\omega_c$, and $\alpha = T_2/\omega_c$, where T_2 is the phonon bath temperature of level 1–2.

APPENDIX B: ENTANGLED STATES OF TWO PHOTONS

The state of spontaneous down conversion (SPDC) to first order in perturbation theory is

$$|\psi\rangle = |0\rangle - \frac{i}{\hbar}\int_{t_0}^{t} dt\,\hat{\mathcal{H}}_I(t)|0\rangle, \tag{B1}$$

where $\mathcal{H}_I$ is the effective third-order interaction Hamiltonian given by

$$\hat{\mathcal{H}}_I(t) = \epsilon_0\int_V d^3\boldsymbol{r}\chi^{(2)}E_p^+(\boldsymbol{r},t)\hat{E}_s^-(\boldsymbol{r},t)\hat{E}_i^-(\boldsymbol{r},t) + \text{H.c.}, \tag{B2}$$

where $\chi^{(2)}$ is the susceptibility tensor of rank 2 which describes the nonlinear crystal. V is the interaction volume covered by the pump field and the pump field is simply chosen as a classical plane wave along the z direction.

$$E_p^+(z,t) = E_p\int d\omega_p\mathcal{A}(\omega_p)e^{-i(k_p(\omega_p)z - \omega_p t)}, \tag{B3}$$

where $\mathcal{A}(\omega_p)$ is the pulse envelope function, and

$$\hat{E}_j^-(z,t) = \int d\omega_j\mathcal{E}(\omega_j)\hat{a}_j^{\dagger}(\omega_j)e^{-i(k_j(\omega_j)z - \omega_j t)}, \tag{B4}$$

where $j = s, i$ and $\hat{a}^{\dagger}(\omega_j)$ is a creation operator, and we have restricted the spatial integral to be over z coordinate only. We assume that $\mathcal{E}(\omega_j) = \sqrt{\hbar\omega/\epsilon_0\mathbf{V}}$, where $\mathbf{V}$ is the quantization volume is slowly varying over the frequencies of interest, and therefore we can bring it outside the integral. The interaction Hamiltonian part of Eq. (B1) using Eqs. (B2), (B3), and (B4) is recast as

$$\int_{t_0}^{t}\mathcal{H}_I(t')dt' = \mathcal{A}\int_{-\infty}^{+\infty}dt'\int_{\frac{-L}{2}}^{\frac{+L}{2}}dz\int d\omega_i d\omega_s d\omega_p \times e^{-i(k_i(\omega_i)+k_s(\omega_s)-k_p(\omega_p))z}e^{i(\omega_s+\omega_i-\omega_p)t}\mathcal{A}(\omega_p) \times \hat{a}_i^{\dagger}(\omega_i)\hat{a}_s^{\dagger}(\omega_s) + \text{H.c.}, \tag{B5}$$

where L is the length of the crystal and $\mathcal{A} = E_p\mathcal{E}(\omega_i)\mathcal{E}(\omega_s)$. For a pulsed laser, we can assume that the pump field, and therefore the interaction Hamiltonian, is zero before t_0 and after t. Therefore, we can extend the limits of the integration over infinite time. Performing the time integral yields $\delta(\omega_i + \omega_s - \omega_p)$, which then allows the ω_p integral to be evaluated, giving

$$\int_{t_0}^{t}\hat{\mathcal{H}}_I(t')dt' = -2\pi\mathcal{A}\int_{\frac{-L}{2}}^{\frac{+L}{2}}dz\int d\omega_i d\omega_s\mathcal{A}(\omega_i+\omega_s) \times e^{-i(k_i(\omega_i)+k_s(\omega_s)-k_p\omega_p)z}\hat{a}_i^{\dagger}(\omega_i)\hat{a}_s^{\dagger}(\omega_s) + \text{c.c.} \tag{B6}$$

Evaluating the integral over z and substituting in Eq. (B1) yields

$$|\psi\rangle = |0\rangle + \frac{2i\pi L\mathcal{A}}{\hbar}\int d\omega_i d\omega_s\mathcal{A}(\omega_i+\omega_s)\Phi(\omega_i,\omega_s) \times \hat{a}_i^{\dagger}(\omega_i)\hat{a}_s^{\dagger}(\omega_s)|0\rangle + \text{H.c.}, \tag{B7}$$

where $\Phi(\omega_i,\omega_s) = \text{sinc}(\frac{L\Delta k}{2})$ and $\mathcal{A}(\omega_s,\omega_i) = \frac{A_0}{\omega_i+\omega_s-\omega_p+i\sigma}$ is the normalized band pump pulse of width σ. For a narrow band pump $\sigma \to 0$.

The essential character of the phase-matching function is better illustrated when it is expressed in a simpler form obtained by making the Taylor expansions

$$k_p(\omega) \approx k_{p0} + (\omega - \bar{\omega})\frac{\partial k_p(\omega)}{\partial\omega}\bigg|_{\omega=2\bar{\omega}},$$
$$k_j(\omega) \approx k_{j0} + (\omega - \bar{\omega})\frac{\partial k_j(\omega)}{\partial\omega}\bigg|_{\omega=\bar{\omega}}. \tag{B8}$$

Here, $2\bar{\omega}$ is the center pump frequency. Discarding all but the first two terms yields, using Eq. (B8),

$$\begin{aligned}\Delta k &= k_s(\omega_s) + k_i(\omega_i) - k_p(\omega_s + \omega_i)\\ &\approx (\omega_s - \omega_i)\left(\frac{\partial k_s(\omega_s)}{\partial \omega_s} - \frac{\partial k_i(\omega_i)}{\partial \omega_i}\right)\\ &= (\omega_s - \omega_i)\left(\frac{1}{v_s} - \frac{1}{v_i}\right).\end{aligned} \tag{B9}$$

Therefore, the phase matching factor reads

$$\Phi(\omega_s, \omega_i) = \mathrm{sinc}\left(\frac{(\omega_s - \omega_i)T}{2}\right), \tag{B10}$$

where $T = L(\frac{1}{v_s} - \frac{1}{v_i})$ is the entanglement time, characterizing the group velocity dispersion inside the SPDC crystal. The output state of SPDC from Eq. (B1) is given by

$$|\psi\rangle = \mathcal{N}A_0 \iint \frac{d\omega_s d\omega_i \Phi(\omega_s, \omega_i)}{\omega_i + \omega_s - \omega_p + i\sigma} \hat{a}_s^\dagger(\omega_s)\hat{a}_i^\dagger(\omega_i)|0\rangle, \tag{B11}$$

where $\mathcal{N}$ is a normalization constant.

For the classical light

$$\begin{aligned}\langle \hat{E}_1^\dagger(\omega_1)\hat{E}_2^\dagger(\omega_2)\hat{E}_2(\omega_2)\hat{E}_1(\omega_1)\rangle &= |\langle 0|\hat{E}_2(\omega_2)\hat{E}_1(\omega_1)|\phi\rangle|^2\\ &= |\mathcal{E}_2(\omega_2)\mathcal{E}_1(\omega_1)|^2.\end{aligned} \tag{B12}$$

where ϕ is a two photon correlated states. Rabi frequency for the transition g–2 via intermediate level e in a given classical field is

$$\begin{aligned}|\Omega_1|^2|\Omega_2|^2 &= |\mu_{eg}|^2|\mu_{2e}|^2|\mathcal{E}(\omega_2)\mathcal{E}(\omega_1)|^2\\ &= |\mu_{eg}|^2|\mu_{2e}|^2|\langle 0|\hat{E}_2(\omega_2)\hat{E}_1(\omega_1)\phi\rangle|^2.\end{aligned} \tag{B13}$$

For quantum light, the two-point field correlation function reads

$$\begin{aligned}\langle 0|\hat{E}_2(\omega_2)\hat{E}_1(\omega_1)|\psi\rangle &= \langle 0|\sqrt{\frac{\omega_s}{2\epsilon_0 V}}\hat{a}_2(\omega_s)\sqrt{\frac{\omega_i}{2\epsilon_0 V}}\hat{a}_1(\omega_i)|\psi\rangle\\ &= \frac{\mathcal{N}}{2\epsilon_0 V}\iint d\omega_s d\omega_i \sqrt{\omega_s\omega_i}\Phi(\omega_s, \omega_i)\\ &\quad\times \frac{A_0}{\omega_i + \omega_s - \omega_p + i\sigma}\\ &\quad\times \langle 0|\hat{a}_2(\omega_s)\hat{a}_1(\omega_i)\hat{a}_i^\dagger(\omega_i)\hat{a}_s^\dagger(\omega_s)|0\rangle\\ &= \frac{A_0\mathcal{N}}{2\epsilon_0 V}\frac{\sqrt{\omega_1\omega_2}}{\omega_1 + \omega_2 - \omega_p + i\sigma}\Phi(\omega_2, \omega_1).\end{aligned} \tag{B14}$$

By combination of Eqs. (B10), (B11), (B13), and (B14) the quantum and correlation functions are recast as

$$\begin{aligned}\Omega_1(\omega_1)\Omega_2(\omega_2) = \frac{\mu_{eg}\mu_{2e}\mathcal{N}A_0}{2\epsilon_0 V}\frac{\sqrt{\omega_2\omega_1}}{\omega_1 + \omega_2 - \omega_p + i\sigma}\\ \mathrm{sinc}\left[\frac{(\omega_2 - \omega_1)T}{2}\right].\end{aligned} \tag{B15}$$

The output power in Eq. (9) using Eq. (14) in the high temperature limit becomes

$$P_Q = \frac{2\,u\,v\,c_{21}\tilde{c}_p\lambda'\,\tau^4\sigma_p'^4\left[2\,\theta\,\tilde{c}_{21} - \tau^4(2\tilde{c}_{21} - c_{21})\sigma_p'^4\right]}{3\left(u\,\tilde{c}_{21}\theta + c_{21}\tau^4\sigma_p'^4\right)\left(v\,\tilde{c}_{21}\theta + c_{21}\lambda'\tau^4\sigma_p'^4\right)}, \tag{B16}$$

where subscript Q denotes the two-photon entangled pump and $\tilde{c}_{21} = \alpha + c_{21}$, $\tilde{c}_p = c_p - c_{21} - 1$, $\theta = \mathrm{sinc}^2[T(\omega_{2e'} - \omega_{ge'})/2]$, $\alpha = T2/\omega_c$, $u = \Gamma_2\omega_c/\Gamma_c T_c$, and $v = \Gamma_c/\omega_c$.

APPENDIX C: MAXIMUM POWER OF QHEs AND SPECTROSCOPY

Using Eq. (20) in the definition of the power of Eq. (8) and applying dimensionless parameters over the high temperature limit, the spectroscopic power is given by

$$\mathcal{P}_C = \frac{4\alpha c_{21}u^2(c_p - c_{21} - 1)\lambda'}{\tau^8\sigma_{\mathrm{pr}}(c_{21} + \alpha u)(c_{21} + 5\alpha u)\sigma_p'^8}, \tag{C1}$$

where all dimensionless parameters were defined in earlier sections. Similarly we recast spectroscopic power for the entangled two-photon source using Eq. (21):

$$\mathcal{P}_Q = \frac{\alpha c_{21}u^2(c_p - c_{21} - 1)\lambda'\mathrm{sinc}^2\left[\frac{T(\omega_{2e'} - \omega_{ge'})}{2}\right]}{2\tau^2\sigma_{\mathrm{pr}}(c_{21} + \alpha u)(c_{21} + 5\alpha u)\sigma_p'^2}. \tag{C2}$$

The maximum output power given in Eqs. (10) and (15) for two-photon entangled and classical states respectively and their numerical simulation vs τ are shown in Fig. 8(a). We considered a small interval of τ because only in this regime are quantum advantages shown in the scale of 10^{-3} and within the range of $\tau \in [0, 0.0048]$, where the maximum output power of the two-photon entangled pump is larger than the two-photon classical pump case. The small value of τ corresponds to the high intensity of the pump field, because $\tau = T_c/T_h$, where $T_h \propto \sqrt{\Omega_p}$ and T_c at room temperature. Similarly, the maximum output power for the spectroscopic regime in Eqs. (22) and (23) is shown in Fig. 8(b) and the quantum advantage is shown in the regime of low pump intensity. The analytical solution of maximum output power in the limit of τ is explained in main text.

[1] S. Carnot, *Réflections sur la Puissance Motrice du Feu et sur les Machines propres à Dévelopeer cette Puissance* (Bachelier Libraire, Paris, 1824).

[2] H. E. D. Scovil, E. O. Schulz-DuBois, Three-Level Masers as Heat Engines, Phys. Rev. Lett. **2**, 262 (1959).

[3] J. E. Geusic, E. O. Schulz-DuBois, and R. W. De Grasse, and H. E. D. Scovil, Three level spin refrigeration and maser action at 1500 mc/sec, J. Appl. Phys. **30**, 1113 (1959).

[4] J. Geusic, E. O. Schulz-Du Bois, H. E. D. Scovil, Quantum equivalent of the carnot cycle, Phys. Rev. **156**, 343 (1967).

[5] E. Geva and R. Kosloff, Three-level quantum amplifier as a heat engine: A study in finite-time thermodynamics, Phys. Rev. E **49**, 3903 (1994).

[6] E. Geva and R. Kosloff, The quantum heat engine and heat pump: An irreversible thermodynamic analysis of the three level amplifier, J. Chem. Phys. **104**, 7681 (1996).

[7] E. Boukobza and D. J. Tannor, Three-Level Systems as Amplifiers and Attenuators: A Thermodynamic Analysis, Phys. Rev. Lett. **98**, 240601 (2007).

[8] V. Singh, Optimal operation of a three-level quantum heat engine and universal nature of efficiency, Phys. Rev. Research **2**, 043187 (2020).

[9] E. Boukobza and D. J. Tannor, Thermodynamics of bipartite systems: Application to light-matter interactions, Phys. Rev. A **74**, 063823 (2006).

[10] F. G. S. L. Brandão, M. Horodecki, J. Oppenheim, J. M. Renes, and R. W. Spekkens, Resource Theory of Quantum States Out of Thermal Equilibrium, Phys. Rev. Lett. **111**, 250404 (2013).

[11] M. N. Bera, A. Riera, M. Lewenstein, and A. Winter, Generalized laws of thermodynamics in the presence of correlations, Nat. Commun. **8**, 2180 (2017).

[12] *Thermodynamics in the Quantum Regime*, edited by F. Binder, L. A. Correa, C. Gogolin, J. Anders, and G. Adesso (Springer, Cham, 2019).

[13] R. Kosloff, A quantum mechanical open system as a model of a heat engine, J. Chem. Phys. **80**, 1625 (1984).

[14] J. Jaramillo, M. Beau, and A. del Campo, Quantum supremacy of many-particle thermal machines, New J. Phys. **18**, 075019 (2016).

[15] W.-K. Mok, K. Bharti, L.-C. Kwek, and A. Bayat, Optimal probes for global quantum thermometry, Commun. Phys. **4**, 62 (2021).

[16] S. Saryal, M. Gerry, I. Khait, D. Segal, and B. K. Agarwalla, Universal Bounds on Fluctuations in Continuous Thermal Machines, Phys. Rev. Lett. **127**, 190603 (2021).

[17] G. Thomas, M. Banik, S. Ghosh, Implications of coupling in quantum thermodynamic machines, Entropy **19**, 442 (2017).

[18] J. Um, K. E. Dorfman, and H. Park, Coherence enhanced quantum-dot heat engine, arXiv:2111.09582.

[19] J. V. Koski, V. F. Maisi, J. P. Pekola, and D. V. Averin, Experimental realization of a Szilard engine with a single electron, Proc. Natl. Acad. Sci. USA **111**, 13786 (2014).

[20] J. Roßnagel, S. T. Dawkins, K. N. Tolazzi, O. Abah, E. Lutz, F. Schmidt-Kaler, and K. Singer, A single-atom heat engine, Science **352**, 325 (2016).

[21] J. Klaers, S. Faelt, A. Imamoglu, and E. Togan, Squeezed Thermal Reservoirs as a Resource for a Nanomechanical Engine beyond the Carnot Limit, Phys. Rev. X **7**, 031044 (2017).

[22] J. P. S. Peterson, T. B. Batalhão, M. Herrera, A. M. Souza, R. S. Sarthour, I. S. Oliveira, and R. M. Serra, Experimental Characterization of a Spin Quantum Heat Engine, Phys. Rev. Lett. **123**, 240601 (2019).

[23] D. von Lindenfels, O. Gräb, C. T. Schmiegelow, V. Kaushal, J. Schulz, M. T. Mitchison, J. Goold, F. Schmidt-Kaler, and U. G. Poschinger, Spin Heat Engine Coupled to a Harmonic Oscillator Flywheel, Phys. Rev. Lett. **123**, 080602 (2019).

[24] J. Klatzow, J. N. Becker, P. M. Ledingham, C. Weinzetl, K. T. Kaczmarek, D. J. Saunders, J. Nunn, I. A. Walmsley, R. Uzdin, and E. Poem, Experimental Demonstration of Quantum Effects in the Operation of Microscopic Heat Engines, Phys. Rev. Lett. **122**, 110601 (2019).

[25] Q. Bouton, J. Nettersheim, S. Burgardt, D. Adam, E. Lutz, and A. Widera, A quantum heat engine driven by atomic collisions, Nat. Commun. **12**, 2063 (2021).

[26] F. Tacchino, A. Auffeves, M. F. Santos, and D. Gerace, Steady State Entanglement beyond Thermal Limits, Phys. Rev. Lett. **120**, 063604 (2018).

[27] G. Manzano, D. Subero, O. Maillet, R. Fazio, J. P. Pekola, and É. Roldán, Thermodynamics of Gambling Demons, Phys. Rev. Lett. **126**, 080603 s (2021).

[28] M. O. Scully, K. R. Chapin, K. E. Dorfman, M. B. Kim, and A. Svidzinsky, Quantum heat engine power can be increased by noise-induced coherence, Proc. Natl. Acad. Sci. USA **108**, 15097 (2011).

[29] A. Ghosh, D. Gelbwaser-Klimovsky, W. Niedenzu, A. I. Lvovsky, I. Mazets, M. O. Scully, and G. Kurizki, Two-level masers as heat-to-work converters, Proc. Natl. Acad. Sci. USA **115**, 9941 (2018).

[30] F. Caravelli, B. Yan, L. P. García-Pintos, and A. Hamma, Energy storage and coherence in closed and open quantum batteries, Quantum **5**, 505 (2021).

[31] K. E. Dorfman, D. V. Voronine, S. Mukamel, and M. O. Scully, Photosynthetic reaction center as a quantum heat engine, Proc. Natl. Acad. Sci. USA **110**, 2746 (2013).

[32] M. O. Scully, Quantum Photocell: Using Quantum Coherence to Reduce Radiative Recombination and Increase Efficiency, Phys. Rev. Lett. **104**, 207701 (2010).

[33] M. O. Scully, M. S. Zubairy, G. S. Agarwal, and H. Walther, Extracting work from a single heat bath via vanishing quantum coherence, Science **299**, 862 (2003).

[34] S. Rahav, U. Harbola, and S. Mukamel, Heat fluctuations and coherences in quantum heat engines, Phys. Rev. A **86**, 043843 (2012).

[35] R. Uzdin, A. Levy, and R. Kosloff, Equivalence of Quantum Heat Machines, and Quantum-Thermodynamic Signatures, Phys. Rev. X **5**, 031044 (2015).

[36] K. Ono, S. N. Shevchenko, T. Mori, S. Moriyama, and F. Nori, Analog of a Quantum Heat Engine Using a Single Spin Qubit, Phys. Rev. Lett. **125**, 166802 (2020).

[37] Md. Qutubuddin and K. E. Dorfman, Incoherent control of optical signals: Quantum-heat-engine approach, Phys. Rev. Research **3**, 023029 (2021).

[38] A. Pechen and H. Rabitz, Teaching the environment to control quantum systems, Phys. Rev. A **73**, 062102 (2006).

[39] F. Schlawin, K. E. Dorfman, B. P. Fingerhut, and S. Mukamel, Suppression of population transport and control of exciton distributions by entangled photons, Nat. Commun. **4**, 1782 (2013).

[40] R. K. Burdick, G. C. Schatz, and T. Goodson III, Enhancing entangled two-photon absorption for picosecond quantum spectroscopy, J. Am. Chem. Soc. **143**, 16930 (2021).

[41] S. Mukamel *et al.*, Roadmap on quantum light spectroscopy, J. Phys. B: At. Mol. Opt. Phys. **53**, 072002 (2020).

[42] Z. Zhang, T. Peng, X. Nie, G. S. Agarwal, and M. O. Scully, Entangled photons enabled time- and frequency-resolved coherent Raman Spectroscopy in condensed phase molecules, arXiv:2106.10988.

[43] K. E. Dorfman, F. Schlawin, and S. Mukamel, Nonlinear optical signals and spectroscopy with quantum light, Rev. Mod. Phys. **88**, 045008 (2016).

[44] O. Varnavski and T. Goodson III, Two-photon fluorescence microscopy at extremely low excitation intensity: The power of quantum correlations, J. Am. Chem. Soc. **142**, 12966 (2020).

[45] S. Rahav and S. Mukamel, Chapter 6 - Ultrafast nonlinear optical signals viewed from the molecule's perspective: Kramers-Heisenberg transition-amplitudess us susceptibilities, Adv. At. Mol. Opt. Phys. **59**, 223 (2010).

[46] D. C. Harris and M. D. Bertolucci, *Symmetry and Spectroscopy: Introduction to Vibrational and Electronic Spectroscopy* (Dover, New York, 1989).

[47] K. E. Dorfman, D. Xu, and J. Cao, Efficiency at maximum power of a laser quantum heat engine enhanced by noise-induced coherence, Phys. Rev. E **97**, 042120 (2018).

[48] R. Kosloff and A. Levy, Quantum heat engines and refrigerators: Continuous devices, Annu. Rev. Phys. Chem. **65**, 365 (2014).

[49] F. Chen and S. Mukamel, Vibrational hyper-Raman molecular spectroscopy with entangled photons, ACS Photonics **8**, 2722 (2021).

[50] F. Schlawin, K. E. Dorfman, and S. Mukamel, Entangled two-photon absorption spectroscopy, Acc. Chem. Res. **51**, 2207 (2018).

[51] A. Svidzinsky, G. Agarwal, A. Classen, A. V. Sokolov, A. Zheltikov, M. S. Zubairy, and M. O. Scully, Enhancing stimulated Raman excitation and two-photon absorption using entangled states of light, Phys. Rev. Research **3**, 043029 (2021).

[52] D. Abramavicius, B. Palmieri, D. V. Voronine, F. Sanda, and S. Mukamel, Coherent multidimensional optical spectroscopy of excitons in molecular aggregates; quasiparticle versus supermolecule perspectives, Chem. Rev. **109**, 2350 (2009).